Proceedings of the ASME 2025
Turbomachinery Technical Conference and Exposition
GT2025
June 16–20, 2025, Memphis, Tennessee

GT2025-153904

INVESTIGATION OF IMPACT OF STEAM ADDITION ON COMBUSTION BEHAVIOR AND POLLUTANT EMISSIONS IN AN RQL COMBUSTOR AT HIGH PRESSURE

Joshua A.T. Gray[1,*], Oliver Lammel[1], Holger Ax[1], Rainer Lückerath[1], Klaus Peter Geigle[1], Greg Boardman[2], Wookyung Kim[3], Matthias Haeringer[4]

[1]German Aerospace Center (DLR), Stuttgart, Germany
[2]Pratt & Whitney, Huntsville, AL
[3]RTX Technology Research Center, East Hartford, CT
[4]MTU Aero Engines, Munich, Germany

ABSTRACT

Emissions reduction in aviation is of paramount importance, due to the associated global warming effects. One way of combating the emissions of NO_x and non-volatile particulate matter is the injection of steam into the combustion reaction. In this study, steam injection successfully reduced the production of both NO_x and soot in a rich-quench-lean (RQL) combustor, which is promising in aircraft engine applications. The tests were conducted at relevant high-pressure (up to 14.4 bar), preheated inlet conditions with kerosene (Jet A-1) as the fuel. In addition to typical pressure, temperature and exhaust gas measurements, additional laser diagnostic techniques (Mie-scattering spray characterization, and laser-induced incandescence) were applied. Furthermore, simultaneous optical emissions measurements of OH (312 nm) and black body radiation of soot (660 nm) provided insight into the locations in the flame for heat release and soot production for various operating conditions with and without steam. These promising results offer a step towards a more complete understanding of the underlying processes of the production of soot in RQL combustors.*

Keywords: combustion, emissions, high-pressure testing, nonintrusive diagnostics

1. INTRODUCTION

Non-CO_2 effects significantly contribute to the overall climate impact of aviation. They are estimated to be responsible for about two-thirds of the global warming potential caused by aviation, although the exact share is still subject to high uncertainty [1]. The two main contributors to the non-CO_2 effects are: nitrogen oxides (NO_x), which act as greenhouse gases when being emitted at high altitude, and non-volatile particulate matter (nvPM) [1], which serve as condensation nuclei for contrail cirrus clouds, which in turn have a net warming effect [2, 3]. The dependence of contrail formation on nvPM emission, especially for low nvPM levels, and their exact climate impact is a field of active research [4, 5]. Nevertheless, Lee et al. [1] indicate that for a typical current aircraft engine, contrails have on average more than twice the climate impact of NO_x emissions. All climate-relevant emissions are combustion (by-)products. While CO_2 is inevitable when burning fossil-based kerosene, the NO_x and nvPM formation and emission crucially depend on combustor technology and operating conditions. One promising way to drastically reduce climate-relevant emissions is MTU's Water-Enhanced Turbofan (WET) concept.

The WET is a revolutionary gas-turbine based concept, which combines the conventional Joule/Brayton cycle with a Clausius-Rankine steam cycle. The gist of this concept is the condensation of water out of the core engine exhaust. The recovered water is pressurized, vaporized and superheated, and injected into the combustion chamber. On the one hand, this process recovers waste heat from the exhaust, offering a potential increase in overall engine efficiency [6, 7]. On the other hand, the available steam can be an effective measure to reduce the formation of NO_x and nvPM in the combustion chamber.

Kaiser et al. [8] estimated the WET potential to a 90 % reduction in NO_x emissions, mainly as a result of steam injection into the combustion chamber, and a 50 % reduction of contrail cirrus radiative forcing, mainly caused by reduced nvPM emissions. Though supported by results obtained in several test rigs [9–12], the estimation of the NO_x reduction potential is hitherto only based on empirical correlations. Regarding nvPM, the estimation focuses on the particle washout in the water recovery unit at the core engine exhaust. The interaction of steam injection with nvPM formation in aircraft engine combustion chambers is vastly unknown.

*Corresponding author: joshua.gray@dlr.de

The present study provides experimental data for the impact of steam injection of NO_x and nvPM emissions of an aircraft engine like rich-quench-lean (RQL) combustor, operated at realistic pressures and temperatures with liquid kerosene. The RQL concept is frequently used in aircraft engines and is a reliable and cost efficient way to achieve low NO_x emissions [13]. It consists of a fuel-rich primary zone, which is then quenched by additional air. Afterwards, the remaining fuel reacts with the additional air in the secondary combustion zone. This avoids the high temperatures associated with stoichiometric combustion, reducing NO production, while maintaining a fairly stable operation compared to lean conditions.

2. EXPERIMENTAL SETUP AND TECHNIQUES

These experiments have been conducted on the high-pressure test rig (HBK-S) of the DLR Institute of Combustion Technology in Stuttgart. The test rig consists of a pressure vessel into which a test carrier is inserted. The test carrier contains the supply lines, combustor hardware, the optically accessible combustion chamber, as well as any necessary instrumentation.

2.1 High-Pressure Test Rig

The high-pressure test rig is used for the investigation of combustor components or scaled burners at gas turbine relevant conditions. It is characterized by extensive optical access for laser diagnostics, which is optimized for the full-scale tests of a single nozzle and for the proper residence time comparable to large-scale gas turbine combustors. Figure 1 shows the optical section, with 3 axial rows of windows on each side. For the tests described here, the first window row (length 441 mm, height 140 mm) correspondes roughly with the flame zone, the second row and third rows (length 160 mm each) allow for further optical access downstream when needed. In the figure, the third row window is replaced by a metal flange. Further necessary instrumentation, such as a suction probe for exhaust gas measurements, can also be installed in these rows. The air and fuel are supplied from the right. Up to five individually controlled air lines may be used, two of which are preheated and used in this study. The exhaust enters the quench section to the left, where it is cooled by quenching water before passing through a traversing nozzle (to set the pressure) and entering the exhaust stack.

The test rig can be operated with pressures up to 40 bar and provides a maximum air mass flow of 1.2 kg/s. The air can be electrically preheated up to 1000 K. A broad spectrum of gaseous and liquid fuels can be tested (natural gas, with propane admixture; synthesis gases: hydrogen, nitrogen; kerosene, light heating oil; etc.), of which natural gas and kerosene were used for the current experiments. The mass flow rates of fuel and air are measured by Coriolis flow meters with an accuracy of approximately $\pm 1\,\%$. The operation conditions of the HBK-S are documented by a live data evaluation system: All data of the standard instrumentation, such as mass flows meters, absolute pressures, pressure differentials, and thermocouple temperatures, are simultaneously displayed at one-second intervals and recorded at five-second intervals. Additional information on the high-pressure test rig can be found in [14].

2.2 Test Carrier and Combustion Chamber

The high-pressure test rig is designed such that a so-called test carrier is mounted to the end flange and inserted into the pressure vessel, where the end flange is bolted, sealing the pressure vessel. The test carrier is shown in Fig. 2. The test carrier features eight sets of double-paned quartz glass windows. This allows optical access on all four sides for both the primary and secondary combustion zones. The preheated front-end air is directed from the upstream side of the test carrier. Preheated quench air is injected between the first and second rows of windows at the top and bottom of the combustion chamber. This partially blocks the laser sheets, as the air manifold is larger than the frame between the windows and the laser sheets are introduced through the top of the test carrier (see, Sec. 3.5), whereas line-of-sight measurements through the side windows have a slightly smaller blockage from the window frame between the primary and secondary combustion zones. The cooling air serves primarily to cool the windows and comes from a third unheated supply. It fills the pressure vessel volume before being forced through openings upstream of the combustion chamber (not seen in figure) where it is directed between the two sets of windows on all sides. It then combines with the combustion products behind the exhaust sampling location.

The test carrier is equipped with circuits for water cooling at 4 bar, 16 bar, and 32 bar, depending on the cooling requirements. The combustion chamber itself is constructed out of copper with integrated cooling channels and is coated with a thermal barrier coating. The temperature of the cooling water is continuously monitored.

In order to monitor for potential thermoacoustic instabilities, measurement locations for dynamic pressure transducers are installed in two locations, in the combustor bulkhead (effusion plate) flush with the combustor dump plane and in the exhaust nozzle. The pressure is transmitted via capillary tube through the end flange and the sensor is located directly outside of the pressure vessel.

A steam generator is used to produce steam at saturation temperature. For these experiments, mass flows of up to 25 g/s were injected into the test carrier. The steam enters the test carrier through the middle of the end flange and is mixed immediately with the front-end air. A static mixer is installed immediately after the gases merge in order to facilitate rapid mixing and homogenization. The preheat temperature of the air is controlled based on a signal from a thermocouple directly upstream of the combustion chamber. This means that as the steam mass flow is increased, a temperature drop in the air–steam mixture is detected and the preheater for the front-end air compensates in order to maintain a constant preheat temperature for the mixture at the combustor entrance.

Finally, although not shown in Fig. 2, there are numerous pressure and temperature measurement positions on the test carrier for absolute pressures, differential pressures, gas temperatures and wall temperatures. The pressures are transmitted via capillary tubes to the respective sensors outside of the pressure vessel and the temperatures are transmitted via K-type thermocouples. These are all routed through the instrumentation ports seen in Fig. 2.

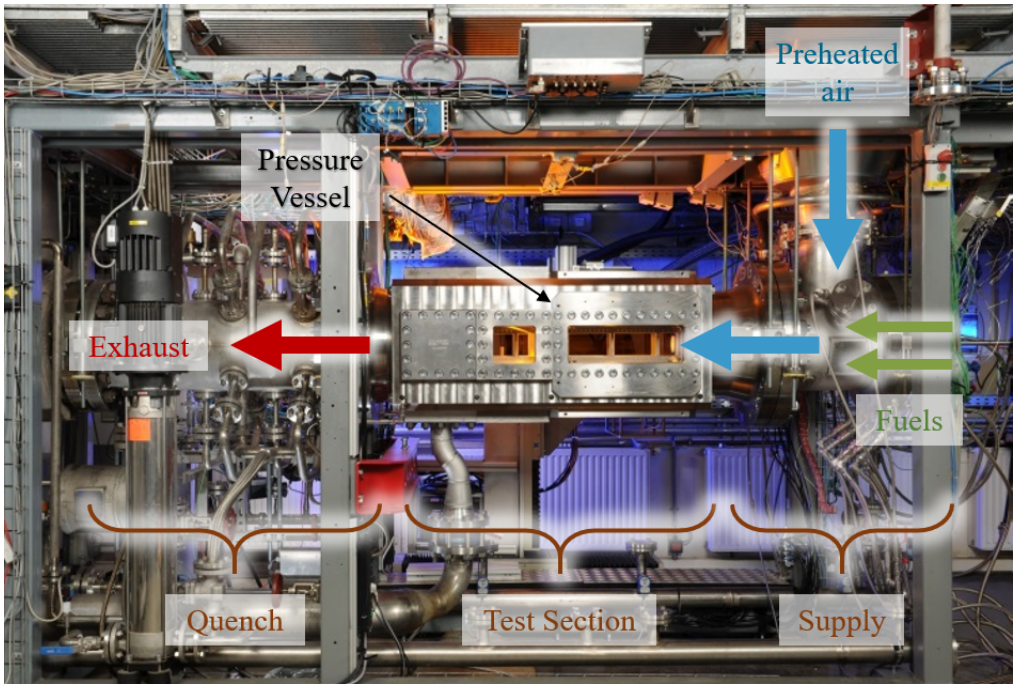

FIGURE 1: HIGH-PRESSURE TEST FACILITY STUTTGART (HBK-S).

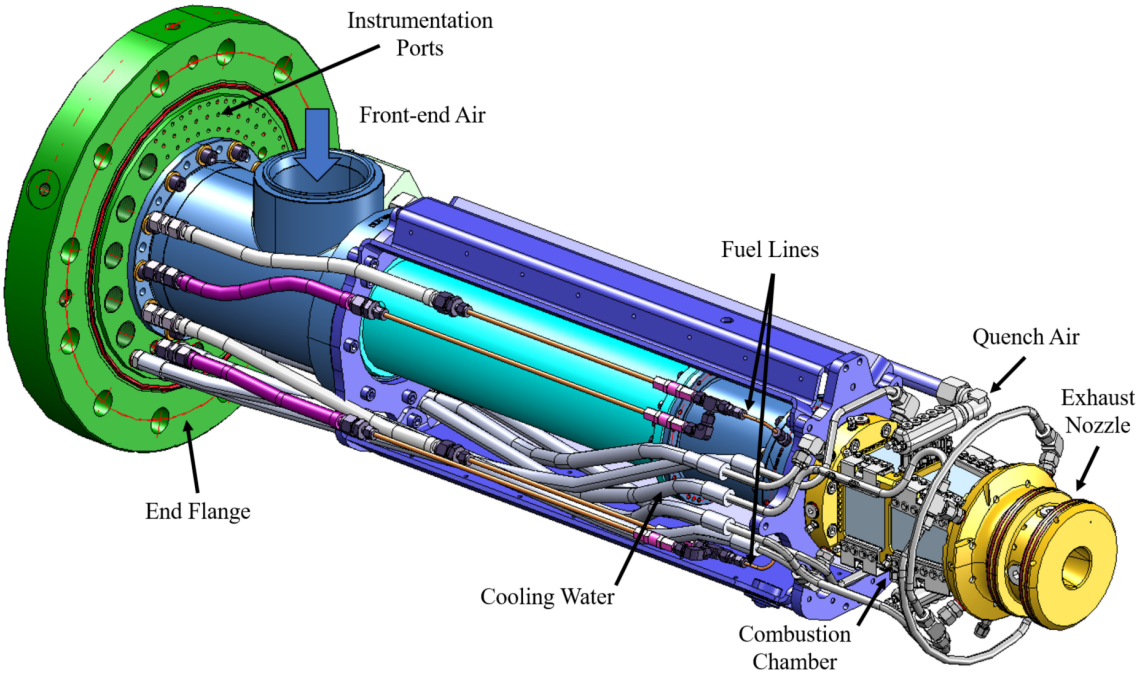

FIGURE 2: TEST CARRIER USED IN THIS MEASUREMENT CAMPAIGN.

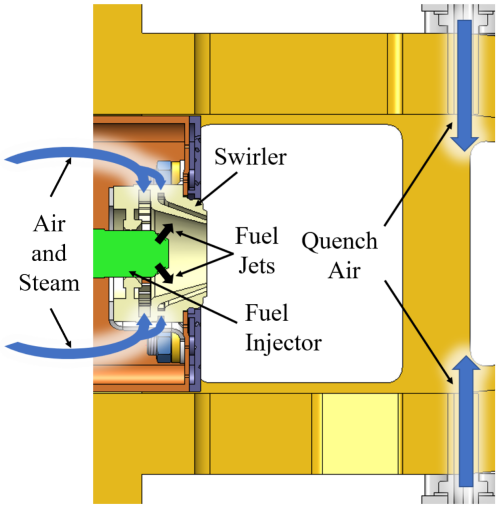

FIGURE 3: SCHEMATIC OF THE COMBUSTION CHAMBER AND ASSEMBLY OF SWIRLER AND FUEL INJECTOR.

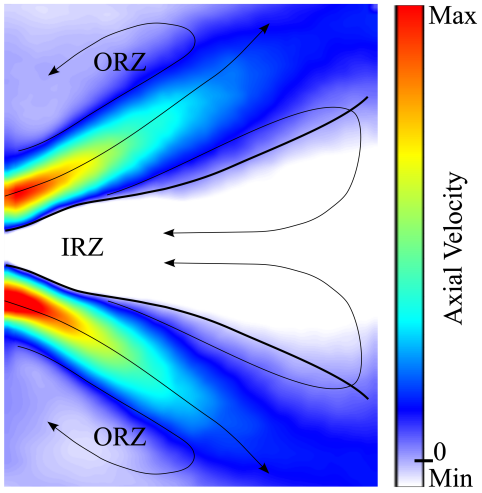

FIGURE 4: SCHEMATIC OF AVERAGE VELOCITY FIELD AT THE CENTER PLANE.

A detailed view of the combustion chamber is shown in Fig. 3. The primary features to note are the swirler, fuel injector, and quench air injector. The bulkhead into which the swirler is installed is effusion cooled. The front-end air is passively distributed through swirler and effusion plate based on effective area. The swirler used in these investigations was a high-shear, compound radial swirler investigated by Cohen and Rosfjord [15], which creates both an inner and outer swirling flow, between which the fuel film is sheared. The specific swirler used in these experiments was based on swirler assembly number 2 found in Tables 1–5 in Cohen and Rosfjord. The only exception is for exemplary results shown in Fig. 8, for which a proprietary swirler was used. The swirler assembly was scaled by Pratt & Whitney using an in-house design tool such that the effective areas resulted in the desired flow distribution between the two swirlers and the effusion cooling as well as the desired velocity field (e.g., bulk velocity) for the DLR combustor at the required test conditions. The swirl is strong enough to create a centralized recirculation domain via vortex breakdown, which improves burner stability. A schematic of a typical non-reacting flow field, with the typical inner and outer recirculation zones, is depicted in Fig. 4.

Kerosene (Jet A-1) is used as the fuel of interest in these studies, although ignition is conducted with natural gas. There are two available fuel circuits in the fuel injector, one for a tip atomizer spray and one for six jet-in-crossflow holes canted to the injector axis. However, in these studies, only the jet-in-crossflow circuit was used. This corresponds to the radial jet nozzle published in Cohen and Rosfjord [15]. The fuel jets impinge upon the outer surface of the inner swirler, producing a fuel film. This film is then sheared between the dual swirling flows.

The quench air is separately controlled and injected through a series of five holes in both the top and bottom of the combustion chamber between the first and second row of windows. The injection holes are each 5 mm in diameter and separated by a distance of 15 mm, with the central hole aligned with and injecting perpendicular to the combustor axis. The injection holes are located approximately 70 mm from the hot-side bulkhead and the top and bottom are aligned so as to produce five sets of opposing, impinging jets. This configuration is generic and has shown to result in reliable burnout, but is not optimized in terms of rapid mixing as would be the case in an industrial RQL combustor.

Ignition is achieved at near atmospheric, but preheated, conditions by laser induced breakdown with the ignition laser focused just downstream of the swirler in the shear layer. Ignition is done exclusively with natural gas. After a stable flame is present, a traversing nozzle is closed in the exhaust stack and flowrates are adjusted to maintain the bulk velocity and front-end equivalence ratio until 8 bar is achieved. Finally, the transition to kerosene is carried out by conducting a stepwise increase in liquid fuel and simultaneous decrease in natural gas over the same fuel line so that during the transition, both gaseous and liquid fuel is present in the same fuel line. This procedure proved to not be a significant challenge. A summary of the operating points for measurements conducted with scaled swirler assembly 2 can be found in Table 1. Subscripts FE refer to front-end conditions, subscripts Q refer to quench conditions, and the global equivalence ratio is given as Φ_{global}.

2.3 Exhaust Gas Analysis

A suction probe with multiple spanwise sampling holes is installed in the exhaust nozzle. The sample is quenched upon entering the probe and then sent over a heated line to a commercial exhaust gas analysis system (ABB Advance Optima). The system records dry concentrations of NO, NO_2, CO, CO_2, and O_2. In order to calculate the emissions in terms of grams of emission gas per kilogram of fuel from parts per million, the following procedure is used:

TABLE 1: OPERATING CONDITIONS FOR MEASUREMENTS CONDUCTED WITH SCALED SWIRLER ASSEMBLY 2

Pressure, bar	$\mathrm{Air}_{\mathrm{FE}}$, g/s	$\mathrm{Steam}_{\mathrm{FE}}$, g/s	T_{FE}, °C	$\mathrm{Air}_{\mathrm{Q}}$, g/s	T_{Q}, °C	Φ_{FE}	Φ_{global}
10.3	89	0.0	491	170	231	0.77	0.26
10.3	89	0.0	491	170	231	1.01	0.35
10.3	89	0.0	491	170	231	1.26	0.43
10.3	89	0.0	491	170	231	1.51	0.52
10.3	89	0.0	491	170	231	1.75	0.60
10.3	89	0.0	491	170	231	2.01	0.70
10.3	89	0.0	491	170	231	2.26	0.77
10.3	89	0.0	491	170	231	2.51	0.86
10.3	89	10.7	491	170	231	0.76	0.26
10.3	89	10.7	491	170	231	1.00	0.34
10.3	89	10.7	491	170	231	1.74	0.60
10.3	89	10.7	491	170	231	2.50	0.86
10.3	89	17.7	491	170	231	1.00	0.34
10.3	89	17.7	491	170	231	1.75	0.60
10.3	89	17.7	491	170	231	2.50	0.86
14.4	121	0.0	521	233	251	1.01	0.35
14.4	121	0.0	521	233	251	1.76	0.60
14.4	121	12.2	521	233	251	1.01	0.35
14.4	121	12.2	521	233	251	1.76	0.60
14.4	121	24.2	521	233	251	1.01	0.35
14.4	121	24.2	521	233	251	1.76	0.60

1. First, the measured mass flowrates in g/s are converted to molar flowrates in mol/s using the molecular weights of dry air, kerosene, and steam.

2. Subsequently, the global combustion reaction is used and balanced for each operation point in order to determine the corresponding molar flowrates for the products CO_2, O_2, N_2, and H_2O. Equation (1) is the generalized stoichiometric combustion reaction for a hydrocarbon with oxygen. This equation is then extended to Equation (2) to include air as the oxydizer as well as steam injection. In this equation, x denotes the molar flowrate of kerosene, y denotes that of air, and z denotes that of steam, taking the global mixture in the combustor into account for each operation point. For the kerosene, an average mixture of $C_{12}H_{23}$ (H:C of 1.917) is assumed for Jet A-1, where $m = 23$ and $n = 12$. Complete combustion is also assumed such that no unburned hydrocarbons remain. This is based on previous experience with this combustor and that the generic secondary air injection was designed specifically for the purpose of complete burnout.

$$\mathrm{C}_n\mathrm{H}_m + (\frac{m}{4} + n)\mathrm{O}_2 + \rightarrow n\mathrm{CO}_2 + \frac{m}{2}\mathrm{H}_2\mathrm{O} \qquad (1)$$

$$x\mathrm{C}_n\mathrm{H}_m + y(0.79\mathrm{N}_2 + 0.21\mathrm{O}_2) + z\mathrm{H}_2\mathrm{O} \rightarrow xn\mathrm{CO}_2 + (y0.21 - \frac{m}{4} + n)\mathrm{O}_2 + (z + \frac{m}{2})\mathrm{H}_2\mathrm{O} + y0.79\mathrm{N}_2 \qquad (2)$$

3. Since the exhaust gas sample is dried before analysis, the reference flowrate of the products for concentration measurements is then the sum of only the flowrates of CO_2, O_2, and N_2. All steam has been removed and all other species are assumed to be negligible with respect to the total flow rate of the products.

4. The dry emissions concentration measurements are then converted from ppm to mol/s using the reference molar flowrate determined in the previous step, then to mass flowrates (g/s), using the respective molecular weights, and finally to grams of emission gas per kilgram of fuel by dividing by the respective mass flow rate of kerosene. NO_x is calculated as the combined masses of NO and NO_2, whereby the mass ratio of NO to NO_2 is also provided for clarity.

2.4 Mie Scattering

Mie scattering is an effective way of visualizing the location of liquid fuel droplets before the vaporization and subsequent combustion is complete. For these measurements, a pulsed frequency-doubled Nd:YAG laser (Innolas Spitlight) with a pulse

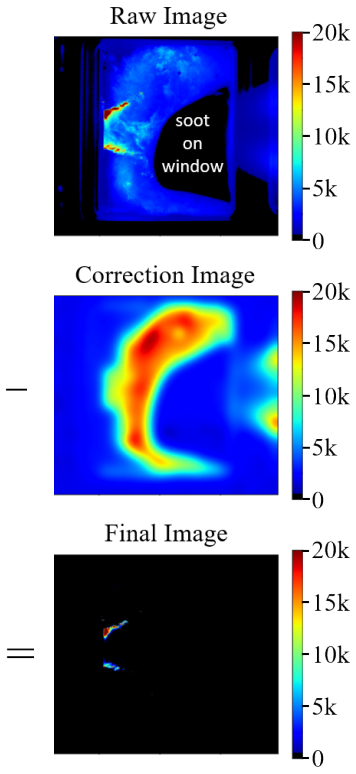

FIGURE 5: IMAGES DETAILING THE DATA ANALYSIS FOR MIE SCATTERING, INCLUDING INSTANTANEOUS RAW IMAGE, CORRECTION IMAGE, AND INSTANTANEOUS FINAL IMAGE.

width of less than 10 ns is used to illuminate the droplets with a wavelength of 532 nm. The laser is steered through an optical array consisting of several mirrors, a cylindrical divergent lens and a cylindrical collimating lens to provide the laser sheet and cylindrical convergent lens to focus the sheet thickness. The locations of the lenses are chosen such that the focal region of the laser sheet is centered in the combustion chamber, resulting in a sheet thickness of approximately 2 mm. The final optics are mounted on a metal profile on the traverse table that extends over the pressure vessel, allowing for the measurement plane to be varied. In this way, a laser sheet is directed into the combustion chamber from above with a mirror, where the fuel droplets are illuminated and the scattered light is recorded on a CMOS camera with a 532 nm filter (full width half maximum ±2 nm). A total of 400 images are recorded at a frequency of 50 Hz and with an exposure time of 20 μs.

Measuring the Mie scattering exclusively from fuel droplets is challenging in an environment with large amounts of soot. First of all, the soot particles emit temperature-dependent, broadband radiation that also includes wavelengths coinciding with those of the band-pass filter at 532 nm. If the radiation is sufficiently intense, these can still be observed. Usually, background image subtraction is sufficient enough to account for this. However, the soot particles also scatter the laser and produce additional signal in this way.

In order to combat this, a dynamic background filter is applied. First, a temporal minimum filter is applied for each individual pixel over all images, resulting in a conservative background image. A multiplication factor for this matrix is then chosen. In the current study, a factor of 8 resulted in a good balance between filter quality and signal loss across all of the desired measurements. Subsequently, a spatial minimum filter with a window size of 51x51 pixels followed by a spatial Gaussian filter of the same window size are applied in succession to the created background image. This final correction image is then subtracted from the instantaneous raw images, from which the mean is calculated, yielding the instantaneous final images that may be subsequently averaged to form the mean image. A sample of these images is given in Fig. 5. Note the visible scattering from soot in the top image, which can be seen in even higher concentrations in some regions. This procedure results in both the soot radiation as well as the Mie scattering from the soot being nearly completely removed with acceptable levels of signal loss (e.g., from the smallest droplets in the dilute spray). For example, the difference in the observed intensity in the average spray before and after filter application is less than 10% and the difference in penetration depth is 1–2 mm for the largest penetration depths.

2.5 Simultaneous OH* Chemiluminescence and Soot Emission Visualization

Imaging of the flame was conducted at 40 Hz and a total of 400 frames were recorded at each operating condition. An image doubler was installed on an intensified CMOS camera in order to obtain simultaneous OH*-chemiluminescence and soot emission images. For the OH*-chemiluminescence images, a band-pass filter at 312 nm with a full width half maximum of ±15 nm was used. The resulting images are a good indication of the location of heat release in the flame. Soot as a broad-band emitter can be detected at any desired wavelength following the criteria (a) avoidance of interference with molecular emissions and (b) desired intensity levels. For the soot emission visualization, a 660 nm bandpass filter was used with a full width half maximum of ±10 nm, which is sufficiently far in the emission spectrum to obtain the desired intensity for the temperatures expected. A neutral density filter (OD1) was additionally used, as the emission for some measurement points was too intense.

2.6 Laser-Induced Incandescence

Laser-induced incandescence (LII) is based on heating soot particles from flame temperatures up to the vaporization temperature by a high-energy laser pulse. The absorbed energy is partially emitted as black body radiation with the intensity maximum shifted to the blue compared to the ambient flame emission. Above a threshold value in laser power the LII radiation intensity is approximately independent of the laser fluence. The soot particle size is expected to be distinctly smaller than the wavelength of the exciting light (Rayleigh regime). Additionally, the primary particles are assumed to be approximately spherical. Because of these two factors, the recorded LII signal is directly proportional to the soot volume fraction. For quantification and determination of the calibration factor, an independent measurement is necessary (typically an extinction experiment). However, for the presented experiment, it was not employed, because the focus is on relative trends. A comprehensive discussion of the method and

its applications can be found in [16, 17] and references therein. Application of LII to pressurized gas turbine combustion has been demonstrated in our own work, for example [18, 19], and elsewhere [20, 21].

The exciting laser for the LII measurements was an Nd:YAG laser (Quantel, Brilliant). The laser beam was steered along the same metal profile as the Mie scattering laser, but through a separate set of optics, and so could also be traversed with the translation tables to obtain different measurement positions. The 10 Hz laser output at 1064 nm was steered into the combustion chamber using several mirrors. A two-lens optics combination (f_{cl} = 80 mm, f_{sph} = 1000 mm) followed by an aperture distributed the laser pulse energy to a 250 μm thick, relatively homogeneous Gaussian sheet in the high fluence LII regime. A final mirror deflected the sheet down into the combustor while the residual transmittance through this mirror was used to monitor the laser sheet quality on a beam profiler mounted on the opposite translation table. The laser sheet energy could alternatively be measured in front of (before the mirror) and behind the combustor, below the bottom window of the pressure vessel. Major factors reducing the laser energy between both positions are scattering due to spray droplets and to a lesser extent absorption, therefore, the pulse energy before the combustor was used to validate values in the LII saturation regime where signal is relatively independent from laser power. Costly operation prevented recording of an extended fluence curve at operating conditions; however, for a stable operating point at 10.3 bar, a fluence variation along four values was performed to validate the use of appropriate fluence values.

The laser fluence of 0.47 J/cm^2 varies by approximately ±25% within the sheet. According to Hofmann et al. [22], fluence curves are relatively unaffected by pressure. Thus, the choice of fluences well above reported typical threshold values for the plateau of the LII response curve under atmospheric conditions (0.2 J/cm^2 according to, for example [23]), considering fluence variations within the sheet profile and from shot to shot appears reasonable. The chosen value also accounts for deterioration of the laser sheet quality inside the combustor due to beam steering caused by strong thermal gradients, as recommended by Zerbs et al. [24].

An ICCD camera (PCO, Dicam Pro) rapidly recorded two images perpendicular to the laser excitation plane, one of soot luminosity and one with the LII signal at 450 nm, each gated at 40 ns. The camera's double frame option allows determining the flame background 500 ns before the laser pulse (i.e., at exactly the same flame conditions). In spite of being weak in intensity, the first frame contains valuable information about the line-of-sight soot distribution of the flame. At every operating condition a sequence of 500 single laser shots was recorded.

3. RESULTS AND DISCUSSION

One concern with the introduction of steam into the combustion was that it would affect the stability of the flame and potentially induce thermoacoustic instabilities for this combustion chamber. This was shown not to be the case at the operating conditions in this study. Observations with a Thorlabs camera and the dynamic pressure transducers showed no indication of thermoacoustic instabilities or any other noticeable indication that the stability of the flame was negatively affected. At leaner front-end conditions, this may still be an issue, however, RQL combustors are not designed to operate in this regime, and therefore, this is largely irrelevant.

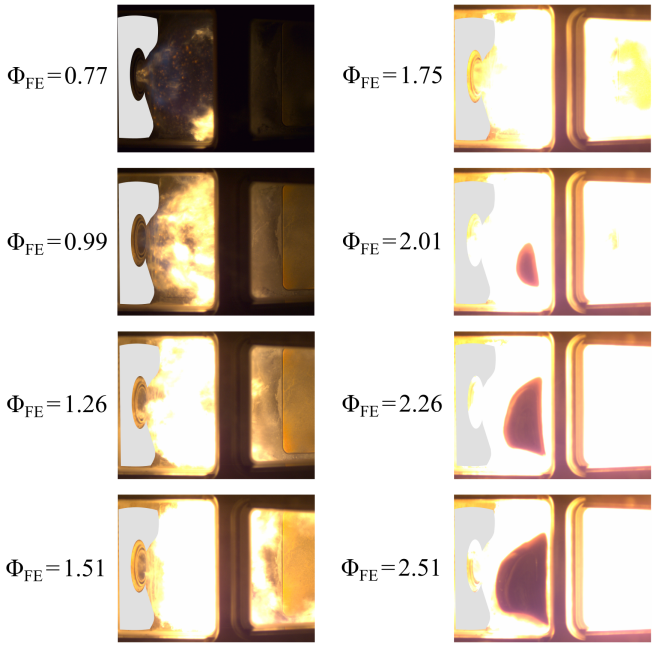

FIGURE 6: IMAGE STILLS OF FLAMES AT 10.3 BAR, SHOWING INCREASED SOOT PRODUCTION AS Φ_{FE} IS INCREASED.

3.1 Flame Visualization

The increase in the amount of soot is clearly evident in still images of the primary flame as the front-end equivalence ratio, Φ_{FE}, is increased. This is shown in Fig. 6 with stills taken using the Thorlabs camera at the same operating conditions except for an increase in Φ_{FE}. These conditions were at 10.3 bar with a front-end air mass flow of 89 g/s preheated to 490°C (763 K) and a quench air mass flow of 170 g/s preheated to 230°C (503 K). The value of Φ_{FE} was varied from approximately 0.75 to 2.5. The effusion hole pattern on the bulkhead are proprietary and are masked in the figure for this reason. The typical glow from the soot increases from lean to rich front-end conditions. Additionally, starting at a front-end equivalence ratio of approximately 2.0, enough soot is present in the flame, that it begins to accumulate on the windows. Returning to leaner conditions results in oxidation of the accumulated soot and it is again removed from the windows.

3.2 Exhaust Gas Analysis

Exhaust gas measurements for NO_x and CO are shown in Fig. 7. These measurements were conducted at 10.3 bar with a front-end air mass flow of 89 g/s. A significant decrease in NO_x is observed due to steam injection, more than a factor of ten at stoichiometric Φ_{FE} and more than a factor of four at the highest values of Φ_{FE}, with respect to emissions per kilogram of fuel. The curve of the operation points without steam is noteworthy, because of the local maximum at a stoichiometric primary zone,

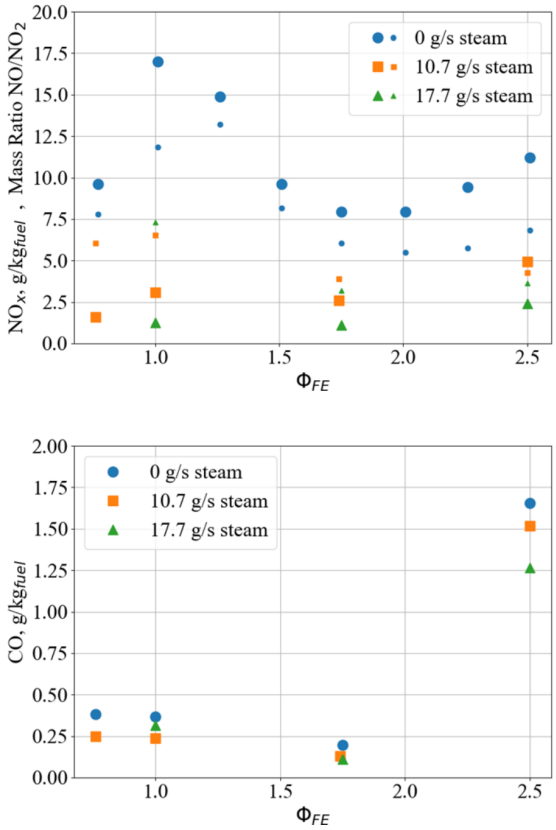

FIGURE 7: EXHAUST GAS MEASUREMENTS FOR NO_x AND CO FOR VARIOUS VALUES OF Φ_{FE} AND STEAM MASS FLOWS. THESE MEASUREMENTS WERE CONDUCTED AT 10.3 BAR AND A FRONT-END AIR MASS FLOW OF 89 G/S. IN THE TOP FIGURE, LARGE SYMBOLS DENOTE NO_x VALUES AND SMALL SYMBOLS DENOTE THE MASS RATIO OF NO TO NO_2.

where the highest local adiabatic flame temperature is expected. As the flame becomes richer, NO_x decreases along with the adiabatic flame temperature until a local minimum is reached. As Φ_{FE} is further increased, the adiabatic flame temperature in the secondary combustion zone increases and with it, a second region of NO_x production is introduced. Therefore, without steam addition, there is potential for the presence of a so-called sweet spot for RQL combustors where a local minimum in NO_x is reached. This region is also perhaps somewhat visible for a steam addition of 10.7 g/s. At the richest front-end conditions, the secondary combustion zone becomes a secondary NO production zone. For the sake of comparison, the conscious decision was made to keep the front end and quench airflows constant. However, in real operation, the quench airflow would likely be increased to keep the NO production in the secondary reaction zone within acceptable limits. However, the benefits of steam addition are clear. In these experiments, very little CO was observed with the exception of the highest values of Φ_{FE}. Here, steam addition appears to have only a moderate impact on emissions reduction.

3.3 Chemiluminescence and Soot Emission

Simultaneous OH*-chemiluminescence and soot emission images were taken for a select few operation points. These points were taken with a proprietary swirler installed rather than that described in Sec. 2.2. Nevertheless, the observations are relevant and worthwhile to report. Four operation points are shown in Fig. 8. Each image is the average of the 400 images recorded. Two points were taken at 10.3 bar with no steam and with 20 % (by mass) steam with respect to front-end air and two points were taken at 14.4 bar, likewise with no steam and with 20 % (by mass) steam with respect to front-end air. These operation points were taken with the goal in mind of keeping the pressure drop across the burner the same for the cases with and without steam. Therefore, the cases without steam compensate with slightly more front-end air (16 %–18 %). This results in the dry operation points being somewhat less rich than their wet counterparts. The front-end equivalence ratios were $\Phi_{FE} = 2.12$ and $\Phi_{FE} = 2.49$ for the 10.3 bar cases, respectively, and $\Phi_{FE} = 1.52$ and $\Phi_{FE} = 1.76$ for the 14.4 bar cases.

Drawing attention first to the cases without steam, the regions of higher intensity for both OH* chemiluminescence and soot emission are located where they are expected; OH* chemiluminescence is located farther upstream where the flame is anchored and soot emission is slightly farther downstream where the production of soot begins to take place. Also, note the secondary combustion zone is fairly elongated. This is likely due to suboptimal mixing of the quench injection air. As mentioned earlier, the design of the quench injection is generic and not optimized. Noticeably, the OH*-emission is more intense at 14.4 bar than at 10.3 bar. This is due to two aspects. First, since the operation points at 14.4 bar are less rich, the flame is closer to stoichiometric and less unburnt fuel persists through the primary zone, leaving less fuel to vaporize and absorb heat from the reaction. Second, the increased density at the higher pressure increases the local concentration of excited OH, which scales linearly with intensity. The secondary reaction zone also appears somewhat shorter, but this is most likely due to the secondary flame being significantly leaner at 14.4 bar as opposed to the flame at 10.3 bar, simply due to the difference in global equivalence ratio, however, pressure effects on flame length may be present.

Without steam, there is markedly more soot in the secondary combustion zone, where soot oxidation is expected to occur, than is to be expected in an RQL combustor. This is also due to the suboptimal mixing of the quench injection, resulting in locally rich pockets and the fact that these data points are somewhat on the rich side of typical RQL operation due to the mass flow of quench air being held constant (as mentioned above). However, the addition of steam results in a significant decrease in the observed soot emission, potentially making these operational points once more viable in regards to acceptable soot production level. The decreased radiative emission can be a result of two factors. First, the concentration of soot can be decreased by the presence of steam due to the chemistry between steam and soot precursors. However, the addition of steam also reduces the adiabatic flame temperature, in turn, reducing the temperature of the soot particles and the associated radiative emissions. The reduction of temperature also influences the chemical soot formation

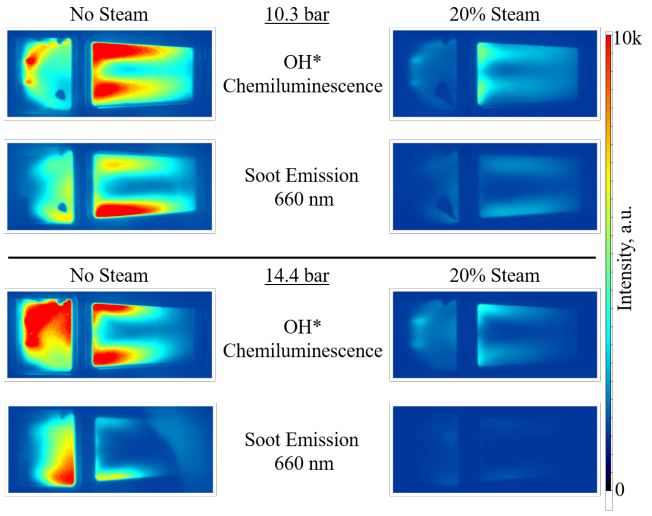

FIGURE 8: AVERAGED SIMULTANEOUS OH*-CHEMILUMINESCENCE AND SOOT EMISSION IMAGES FOR OPERATION POINTS AT 10.3 BAR AND 14.4 BAR WITHOUT STEAM AND WITH 20% (BY MASS) STEAM WITH RESPECT TO FRONT-END AIR.

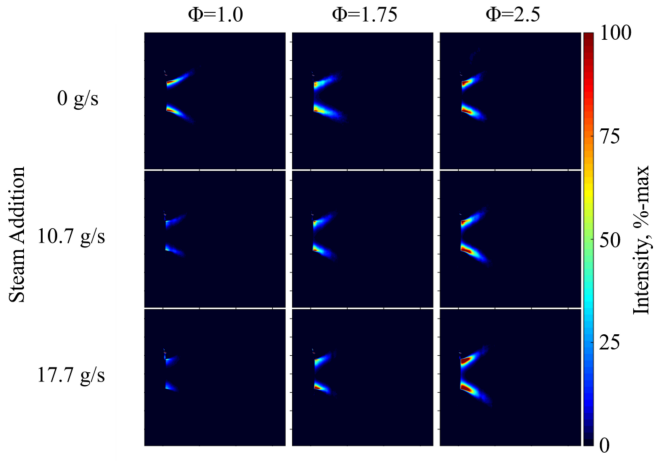

FIGURE 9: AVERAGE MIE SCATTERING IMAGES FOR OPERATION POINTS WITH VARYING LEVEL OF STEAM AND Φ_{FE}.

pathways. This underscores the need to perform additional LII experiments, in which only the presence of soot independent of temperature is observed, in order to confirm this behavior.

3.4 Mie Scattering

With Mie scattering, the injection and vaporization of the kerosene can be observed with respect to equivalence ratio and steam addition. One such dependence is shown in Fig. 9. This operation point is again at 10.3 bar with a front-end air mass flow rate of 89 g/s preheated to 491°C (764 K) and a quench air mass flow rate of 170 g/s preheated to 231°C (504 K). The front-end equivalence ratios shown (Φ_{FE} = 1.0, 1.75, 2.5) correspond to global equivalence ratios of 0.34, 0.6, and 0.86, respectively.

As Φ_{FE} is increased, the penetration depth as well as the width of the fuel jets generally increases. Furthermore, with the exception of the operating conditions at $\Phi_{FE} = 2.5$, addition of steam allows for a more rapid vaporization of the fuel, as seen by the decrease in penetration depth as the steam mass flow is increased. This is due to the fact that the additional steam, at the same inlet temperature as the air, contributes significant energy to the vaporization process, having a higher heat capacity than air. In the immediate vicinity of the droplets, heating of the kerosene significantly reduces the temperature of the air at the liquid–gas interface. With the higher heat capacity of stream, more energy is locally available to be transferred to the kerosene droplets. Thus, the steam improves the processes of atomization and vaporization. This, in turn, improves mixing, as the gas–liquid interface surface is decreased and less diffusion combustion takes place. Furthermore, the addition of 10 % –20 % steam by mass has a disproportionately higher effect on velocity in the vicinity of the fuel nozzle than one may initially expect, because the density of steam is roughly half that of air at the same temperature and pressure. The associated increase in velocity also increases atomization of the fuel droplets. These two factors together have the potential to significantly reduce soot formation.

3.5 Laser-Induced Incandescence

Similar to the visual impression and luminosity images shown thus far, the LII images show a significant and quantifiable reduction of soot presence inside the combustor when adding steam. The following Fig. 10 and Fig. 11 show the range of observed factors of reduction. Fig. 10 shows the impact of steam addition for a 10.3 bar case at a Φ_{FE} of 1.75. The top row contains the representation of the dry case, the bottom row upon injection of 12 % (by mass) steam. In all cases, soot deposits are visible on the inner combustor windows. Since the LII camera was placed at the opposite side of the combustor and the rectangular combustor provides a four-fold symmetry, those deposits appear at the top of the window, in contrast to the plots shown in Fig. 8.

The left part of the image shows soot luminosity as recorded with the first frame of the dual-exposure ICCD camera employed for LII. The individual LII images, recorded in the second frame, are corrected for this background luminosity on an instantaneous basis. Qualitatively, this luminosity relates to the information shown in Fig. 8, yet recorded with a different filter. The right part of the image shows the soot distribution along the central plane of the combustor as visualized with LII and reveals more detail than the line-of-sight integrated soot luminosity. The soot distribution forms an envelope around the spray cone visualized by Mie scattering (Fig. 9) which physically can be explained by the time lag between atomization/mixing and soot formation. The LII image of the primary combustion zone shows a stipe structure which is due to defects on the laser entry window. For the shown dry reference case, soot penetrates into the downstream segment where it subsequently gets oxidized when the global stoichiometry becomes lean after mixture with the added quench air. At wet conditions (12 % steam addition by mass, bottom row) the same arbitrary intensity scale is used. Soot luminosity as well as LII signal are barely visible at those conditions, indicating a soot reduction of two orders of magnitude for this case. Further

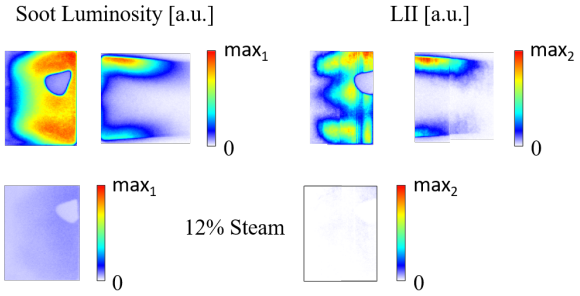

FIGURE 10: SOOT LUMINOSITY AND LII IMAGES FOR OPERATION POINTS AT 10.3 BAR WITHOUT STEAM AND WITH 12 % (BY MASS) STEAM WITH RESPECT TO FRONT-END AIR, Φ_{FE} = 1.75.

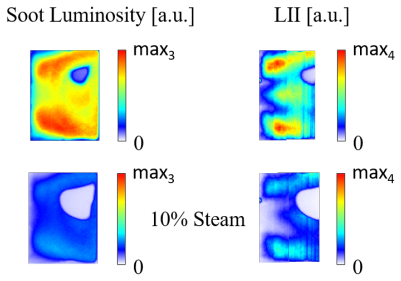

FIGURE 11: SOOT LUMINOSITY AND LII IMAGES FOR OPERATION POINTS AT 14.4 BAR WITHOUT STEAM AND WITH 10 % (BY MASS) STEAM WITH RESPECT TO FRONT-END AIR, Φ_{FE} = 1.75.

addition of steam at 20 % further reduces signal intensities to noise levels (not shown).

Figure 11 shows the soot luminosity and LII for a higher pressure of 14.4 bar and the same equivalence ratio. The shape of the distributions is identical to those shown for the 10.3 bar case (Fig. 10). However, the reduction of soot is far less than for the presented 10.3 bar case, yet significant. While the soot luminosity images (left) are difficult to use for quantification due to their line-of-sight character, the comparison on basis of the LII images indicates a reduction by roughly a factor of three. For the other studied operation conditions, soot reduction was between those extremes. A reason for this wide range is out of the scope of the present paper and shall be explored in more detail in follow-up work digging into details of the instantaneous distributions of all operating points.

Fig. 12 provides a representation of the dynamics of soot formation which — unlike the spray distribution, which is locally quite stable — strongly depends on local turbulence combined with survival times of rich fluid elements prior to mixing with leaner streaks. The figure features a set of instantaneous LII images, belonging to the dry combustion case shown in Fig. 10 (top right, primary combustion segment). Peak intensities of the instantaneous images are higher by roughly one order of magnitude compared to the time averages shown in Fig. 10. The reason for this is evident from the set of subsequent images, which fluctuate in peak intensity as well as in soot filament location, shape and extension. A feature in common with the time average is the probable presence of soot in the top and bottom region close

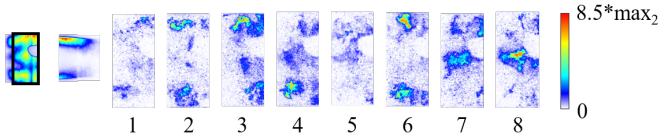

FIGURE 12: INDIVIDUAL LII IMAGES SHOWING THE HIGHLY-DYNAMIC CHARACTER OF SOOT FORMATION. OPERATION POINT OF 10.3 BAR WITHOUT STEAM, Φ_{FE} = 1.75. THE MEASUREMENT POSITION IS SHOWN ON THE SPLICED AVERAGE SIGNAL (LEFT).

to the combustor windows and along the combustor axis. The high dynamics visualized in the instantaneous soot distributions and the non-linear behavior of soot formation evidences the importance of consideration of a wide range of local mixing states and time histories in numerical simulation of soot formation in technical devices.

4. CONCLUSION

Despite concerns that steam injection could compromise flame stability in this burner, in reality, the flames were actually quite stable both in terms of flame stabilization as well as thermoacoustics, even in very rich regimes. Steam injection showed a moderate reduction in CO at the highest values of Φ_{FE} and a significant reduction of NO_x across the board, ranging from factor of four to more than a factor of ten depending on the operating conditions. Soot reduction was observed anywhere from a factor of three up to two orders of magnitude. The scope of this paper was to present an overview with a demonstration of steam addition in a high-pressure RQL burner. A deeper understanding of the underlying processes is the goal of future works.

ACKNOWLEDGMENTS

The authors like to thank for the received funding of the project SWITCH from the Clean Aviation Joint Undertaking of the European Union's Horizon Europe research and innovation programme, under the grant agreement number 101102006.

The authors would also like to thank the team at HBKS: Timo Schiek and Steffen Peukert for assembly and modifications of the test carrier and Thomas Gall and Roman Schieferstein for operation and maintenance of the test rig.

Furthermore, the authors would like to thank Anes Asmi and David Nottebaum for data analysis and preparation of figures for this publication.

REFERENCES

[1] Lee, D.S., Fahey, D.W., Skowron, A., Allen, M.R., Burkhardt, U., Chen, Q., Doherty, S.J., Freeman, S., Forster, P.M., Fuglestvedt, J., Gettelman, A., De León, R.R., Lim, L.L., Lund, M.T., Millar, R.J., Owen, B., Penner, J.E., Pitari, G., Prather, M.J., Sausen, R. and Wilcox, L.J. "The Contribution of Global Aviation to Anthropogenic Climate Forcing for 2000 to 2018." *Atmospheric Environment* Vol. 244 (2021): 117834. DOI 10.1016/j.atmosenv.2020.117834.

[2] Kärcher, B. "Formation and Radiative Forcing of Contrail Cirrus." *Nature Communications* Vol. 9 (2018): 1824. DOI 10.1038/s41467-018-04068-0.

[3] Voigt, C., Kleine, J., Sauer, D., Moore, R.H., Bräuer, T., Le Clercq, P., Kaufmann, S., Scheibe, M., Jurkat-Witschas, T., Aigner, M., Bauder, U., Boose, Y., Borrmann, S., Crosbie, E., Diskin, G.S., DiGangi, J., Hahn, V., Heckl, C., Huber, F., Nowak, J.B., Rapp, M., Rauch, B., Robinson, C., Schripp, T., Shook, M., Winstead, E., Ziemba, L., Schlager, H. and Anderson, B.E. "Cleaner Burning Aviation Fuels can Reduce Contrail Cloudiness." *Communications Earth & Environment* Vol. 2 (2021): 114. DOI 10.1038/s43247-021-00174-y.

[4] Märkl, R. S., Voigt, C., Sauer, D., Dischl, R. K., Kaufmann, S., Harlaß, T., Hahn, V., Roiger, A., Weiß-Rehm, C., Burkhardt, U., Schumann, U., Marsing, A., Scheibe, M., Dörnbrack, A., Renard, C., Gauthier, M., Swann, P., Madden, P., Luff, D., Sallinen, R., Schripp, T. and Le Clercq, P. "Powering aircraft with 100 % sustainable aviation fuel reduces ice crystals in contrails." *Atmospheric Chemistry and Physics* Vol. 24 (2024): 3813–3837. DOI 10.5194/acp-24-3813-2024.

[5] Yu, F., Kärcher, B. and Anderson, B.E. "Revisiting Contrail Ice Formation: Impact of Primary Soot Particle Sizes and Contribution of Volatile Particles." *Environmental Science & Technology* Vol. 58 (2024): 17650–17660. DOI 10.1021/acs.est.4c04340.

[6] Schmitz, O., Klingels, H. and Kufner, P. "Aero Engine Concepts Beyond 2030: Part 1—The Steam Injecting and Recovering Aero Engine." *Journal of Engineering for Gas Turbines and Power* Vol. 143 (2021): 021001. DOI 10.1115/1.4048985.

[7] Ziegler, P., Kaiser, S. and Gümmer, V. "Parametric Cycle Studies of the Water-Enhanced Turbofan Concept." *Turbo Expo: Power for Land, Sea, and Air* (2023): GT2023-1000529, DOI 10.1115/GT2023-100529.

[8] Kaiser, S., Schmitz, O., Ziegler, P. and Klingels, H. "The Water-Enhanced Turbofan as Enabler for Climate-Neutral Aviation." *Applied Sciences* Vol. 12 (2022): 12431. DOI 10.3390/app122312431.

[9] Chen, A. G., Maloney, Daniel J. and Day, William H. "Humid Air NOx Reduction Effect on Liquid Fuel Combustion." *Journal of Engineering for Gas Turbines and Power* Vol. 126 (2004): 69–74. DOI 10.1115/1.1615255.

[10] Schimek, S., Göke, S. and Paschereit, C. "Emission Formation of Liquid Fuel Combustion under Humidified Conditions." *51st AIAA Aerospace Sciences Meeting* (2013): AIAA2013-0693, DOI 10.2514/6.2013-693.

[11] Furuhata, T., Kawata, T., Mizukoshi, N. and Arai, M. "Effect of Steam Addition Pathways on NO Reduction Characteristics in a Can-Type Spray Combustor." *Fuel* Vol. 89 (2010): 3119–3126. DOI 10.1016/j.fuel.2010.05.018.

[12] Crayford, A., Bowen, P., Durand, E., Pugh, D., Sevcenco, Y. and Johnson, M. "Influence of Humidity and Fuel Hydrogen Content on Ultrafine Non-Volatile Particulate Matter Formation in RQL Gas Turbine Technology." *Turbo Expo: Power for Land, Sea, and Air* (2020): GT2020-15168, DOI 10.1115/GT2020-15168.

[13] McKinney, R.G., Sepulveda, D., Sowa, W. and Cheung, A.K. "The Pratt & Whitney TALON X Low Emissions Combustor: Revolutionary Results with Evolutionary Technology." *45th AIAA Aerospace Sciences Meeting and Exhibit* (2007): AIAA 2007-386, DOI 10.2514/6.2007-386.

[14] Lammel, O., Schütz, H., Schmitz, G., Lückerath, R., Stöhr, M., Noll, B., Aigner, M., Hase, M. and Krebs, W. "FLOX® Combustion at High Power Density and High Flame Temperatures." *Journal of Engineering for Gas Turbines and Power* Vol. 132 (2010): p. 121503. DOI 10.1115/1.4001825.

[15] Cohen, J.M. and Rosfjord, T.J. "Influences on the Sprays Formed by High-Shear Fuel Nozzle/Swirler Assemblies." *Journal of Propulsion and Power* Vol. 9 (1993): 16–27. DOI 10.2514/3.51351.

[16] Santoro, R.J. and Shaddix, C.R. "Laser-Induced Incadescence." *in. K. Kohse-Höinghaus, J.B. Jeffries (Eds.) Applied Combustion Diagnostics, Taylor & Francis, New York* (2002): 252.

[17] Michelsen, H. A., Schulz, C., Smallwood, G. J. and Will, S. "Laser-induced incandescence: Particulate diagnostics for combustion, atmospheric, and industrial applications." *Progress in Energy and Combustion Science* Vol. 51 (2015): 2–48. DOI 10.1016/j.pecs.2015.07.001.

[18] Geigle, K.P., Köhler, M., O'Loughlin, W. and Meier, W. "Investigation of soot formation in pressurized swirl flames by laser measurements of temperature, flame structures and soot concentrations." *Proc. Combust. Inst.* Vol. 35 (2015): 3373–3380. DOI 10.1016/j.proci.2014.05.135.

[19] Geigle, K.P., Zerbs, J., Hadef, R. and Guin, C. "Laser-induced incandescence for soot measurements in an aero-engine combustor at pressures up to 20 bar." *Appl. Phys. B* Vol. 125 (2015): 96. DOI 10.1007/s00340-019-7211-2.

[20] Perrier, A., Milea, A.-S., Caceres, M., Vandel, A., Godard, G., Cayre, A., Collin-Bastiani, F., Cabot, G. and Grisch, F. "Soot Formation and Flame Characterization in a Swirl Kerosene Spray Rich Burn-Quench-Lean Burner at Elevated Pressure." *Turbo Expo: Power for Land, Sea, and Air* (2023): GT2023-103642, DOI 10.1115/GT2023-103642.

[21] McGrath, R., Juergensmeyer, J., Bond, R., Bugay, E., Wehe, S., Wu, D., Steinberg, A., Sun, W. and Mazumdar, Y.C. "Planar laser-induced incandescence for the study of soot production in a multi-sector RQL Jet A combustor." *Applications in Energy and Combustion Science* Vol. 18 (2024): 100269. DOI 10.1016/j.jaecs.2024.100269.

[22] Hofmann, M., Bessler, W.G., Schulz, C. and Jander, H. "Laser-induced incandescence for soot diagnostics at high pressures." *Applied Optics* Vol. 42 (2003): 2052–2062. DOI 10.1364/AO.42.002052.

[23] Michelsen, H.A., Schrader, P. E. and Goulay, F. "Wavelength and temperature dependences of the absorption and scattering cross sections of soot." *Carbon* Vol. 48 (2010): 2175-2191. DOI 10.1016/j.carbon.2010.02.014.

[24] Zerbs, J., Geigle, K. P., Lammel, O., Hader, J., Stirn, R., Hadef, R. and Meier, W. "The influence of wavelength in extinction measurements and beam steering in laser-induced incandescence measurements in sooting flames." *Applied Physics B* Vol. 96 (2009): 683–694. DOI 10.1007/s00340-009-3550-8.